

Research Article

T-Shaped Control Plate Effect on Flow past a Square Cylinder at Low Reynolds Numbers

Maryam Shahab,¹ Shams Ul-Islam^{ID,1} and Ghazala Nazeer²

¹Department of Mathematics, COMSATS University Islamabad, Islamabad 44000, Pakistan

²The Government Sadiq College Women University, Bahawalpur 63000, Pakistan

Correspondence should be addressed to Shams Ul-Islam; islam_shams@comsats.edu.pk

Received 7 October 2021; Revised 31 October 2021; Accepted 22 November 2021; Published 2 December 2021

Academic Editor: Ahmed Zeeshan

Copyright © 2021 Maryam Shahab et al. This is an open access article distributed under the Creative Commons Attribution License, which permits unrestricted use, distribution, and reproduction in any medium, provided the original work is properly cited.

In this study, the influence of the T-shaped control plate on the fluid flow characteristics around a square cylinder for a low Reynolds numbers flow is systematically presented. The introduction of upstream attached T-shaped control plate is novel of its kind as T-shaped control plate used for the first time rather than the other passive control methods available in the literature. The Reynolds numbers (Re) are chosen to be $Re = 100, 150, 200$, and 250 , and the T-shaped control plate of the same width with varying length is considered. A numerical investigation is performed using the single-relaxation-time lattice Boltzmann method. The numerical results reveal that there exists an optimum length of T-shaped control plate for reducing fluid forces. This optimum length was found to be 0.5 for $Re = 100, 150$, and 200 and 2 for $Re = 250$. At this optimum length, the fluctuating drag forces acting on the cylinder are reduced by 134% , 1375% , 133% , and 136% for $Re = 100, 150, 200$, and 250 , respectively. Instantaneous and time-averaged flow fields were also presented for some selected cases in order to identify the three different flow regimes around T-shaped control plate and square cylinder system.

1. Introduction

Controlling of flow and suppression of fluid forces around bluff bodies is an important research area for engineers and scientists because of its practical importance in mechanical engineering, structures and buildings, aeronautical engineering etc., at high Reynolds number (Re). Applications at very low Reynolds number can be found in microdevices, such as in micro-electro-mechanical systems (MEMS), computer equipment's, and cooling of electronic devices. The flow past circular cylinders was mostly encountered in the earlier investigations. Among other bluff structures, square structure plays an important role in various engineering fields. The flow wake around the bluff structures can generate unsteady forces which have the potential to damage the structural integrity. Therefore, it is important to fully understand the flow characteristics and their resulting effects on the structure in order to control the structure integrity. Successful numerical simulation can show valuable flow

characteristics and information which can be very complicated to attain experimentally.

Successful flow control remarkably reduces the magnitude and effects of the fluctuating forces directly acting on the surfaces of the bluff body. One can use either active or passive techniques to control the wake and reduce the fluid forces. The passive technique does not require any external energy like the active technique. The previous experimental measurements and numerical studies for flow control include splitter plates [1–10] and control cylinders/rods [11–18] for Re between 80 and 2000 . The development of passive methods of reduction of fluid forces and wake control is an active area of research.

Abdi et al. [1] numerically studied the flow characteristics over a circular cylinder using the commercial software COMSOL Multiphysics. It was concluded that single splitter plate and two splitter plates reduce the drag by about 15% and 23% , respectively. Islam et al. [2] studied numerically the reduction of fluid forces for flow past a square cylinder in the

presence of upstream, downstream, and dual splitter plates. The authors found that the drag force was reduced by up to 62.2%, 13.3%, and 70.2% for upstream, downstream, and dual splitter plates, respectively. Zhou et al. [3] experimentally observed that the upstream rigid splitter plate does not considerably reduce forces. Sharma and Eswaran [4] experimentally studied the flow past a square cylinder in presence of an attached flexible splitter plate at $Re = 400$. The authors observed that the drag coefficient varies non-monotonically due to various flow regimes. The experimental investigation was conducted to study the effect of an attached splitter plate on the rear side of the square cylinder at $Re = 485$ by Chauhan et al. [5]. They found 23% drag reduction and also found that the vortex shedding starts to suppress for the long length of the splitter plate. Dash et al. [6] numerically examined the fluid forces for flow past a square cylinder in presence of dual attached splitter plates. It was found that the drag was reduced by 21% for $Re = 100$. Soumya and Prakash [7] numerically studied the effect of downstream attached splitter plate with elliptic cylinder for Re between 50 and 200 using Streamline Upwind/Petrov-Galerkin (SUPG) based finite element method (FEM). It was concluded that the drag forces were significantly reduced as the length of the splitter plate increased. Several two-dimensional numerical investigations have thus been adopted in studies for the reduction of fluid forces using rigid, flexible, and dual splitter plates (e.g., Barman and Bhattacharyya [8], Sharma and Dutta [9], and Sarioglu [10]).

A numerical study on a flow past a circular cylinder in the presence of a control cylinder was carried out by Kim et al. [11]. They discussed in detail the flow characteristics by changing the positions of the control cylinder.

Islam et al. [12] numerically observed that the upstream control plate considerably reduced the drag forces and the shedding frequency for Re varying between 80 and 200 for flow past a square cylinder. Sharma and Dutta [13] experimentally examined the flow past a square cylinder in the presence of attached flexible foil, for different values of flexible foil length. Firat et al. [14] numerically examined the influence of a small control cylinder at the front of the square cylinder for various Reynolds numbers ($50 \leq Re \leq 200$), and it was found that the drag reduction occurs at gap spacing, $g = s/D = 2$ and 3. Here, s is the spacing between the control cylinder and the main square cylinder, and D is the size of the square cylinder. Yen et al. [15] experimentally examined the flow regimes, drag coefficient, lift coefficient, turbulence intensity, and vortex shedding frequency behind a square cylinder in the presence of an upstream control bar by varying the values of Re , rotation angles, and g values. They found that the upstream control bar reduces drag by about 57%. Zhu and Yao [16] numerically analyzed the effect of surrounding control cylinders for flow over a circular cylinder at intermediate Reynolds numbers. Different small control rods with the same diameter are placed around the main circular cylinder with uniform angle interval (θ) and gap spacing. For example, for four control rods, the angle interval is 9° . The authors found that the main circular cylinder attached to nine control rods with $\theta = 40^\circ$ and $g = 0.6$ can achieve a considerable vortex-induced vibration

suppression effect for a wide range of Reynolds numbers. A numerical study on a flow past a square cylinder in the presence of control rods was carried out by Zhu et al. [17] and Chauhan et al. [18]. They discussed in detail the suppression of vortex shedding and reduction of fluid forces. When one bluff body is placed in the wake of another bluff body, the fluid flow characteristics considerably depend on the gap spacing between the bluff bodies. Some representative numerical studies are those of Abbasi et al. [19] and Ahmad and Islam [20]. Abbasi et al. [19] numerically examined the flow fields and fluid forces around three inline cylinders and found considerable drag reduction for the downstream cylinders. Ahmad and Islam [20] observed various flow regimes and sensitivity of fluid forces for four cylinders in diamond arrangements. For a review of the various passive and active methods of drag reduction, the reader is referred to Rashdi et al. [21].

The flow past a square cylinder in the presence of an upstream attached T-shaped control plate is not studied yet. It is important to know how to control the wake and reduce the fluid forces with the different length of the upstream attached T-shaped control plate. The main motivation for the current work is to examine in detail whether the T-shaped control plate considerably reduced the fluid forces and suppressed the vortex shedding? Also, we aim to characterize wake structure behavior, as a function of the length of T-shaped control plate and Reynolds numbers. The other important aim is to identify the suitable length of the T-shaped control plate that is associated with minimum drag and maximum suppression of vortex shedding. To get reasonably reliable knowledge of important design parameters such as drag and lift forces, vortex shedding frequency, and wake size is very important. We believe that this study will further enrich the drag reduction database using a new passive technique (T-shaped control plate).

The paper is organized as follows. In Section 2, lattice Boltzmann method, problem description, boundary conditions, grid independence study, domain independence study, and validation of the developed code are presented with brief discussion. Section 3 includes the numerical results in detail. Finally, in Section 4, conclusions are drawn based on the present numerical results.

2. Lattice Boltzmann Method and Computational Details

Recently, the lattice Boltzmann method (LBM) has been applied successfully to a number of flow problems (see [19, 20] and some references cited in those works). The LBM is a compressible method, the Mach number, $Ma = U_\infty / \sqrt{RT}$ is set to less than 0.3 so that the compressible effect is negligible [22]. The reason is that we are interested in isothermal flow. In case of isothermal flow, $RT = 1/3$ is to be chosen in the units of $c = \delta x / \delta t = 1$. Here, $c = \delta x / \delta t$, δx , and δt are the lattice constant and the time step size, respectively. The governing differential equations for such fluid flow problems mainly consist of the equations of continuity and momentum, as follows:

Continuity:

$$\frac{\partial u_x}{\partial x} + \frac{\partial u_y}{\partial y} = 0. \quad (1)$$

Momentum:

$$\frac{\partial u_x}{\partial t} + u_x \frac{\partial u_x}{\partial x} + u_y \frac{\partial u_x}{\partial y} = -\frac{\partial p}{\partial x} + \frac{1}{\text{Re}} \left(\frac{\partial^2 u_x}{\partial x^2} + \frac{\partial^2 u_x}{\partial y^2} \right), \quad (2)$$

$$\frac{\partial u_y}{\partial t} + u_x \frac{\partial u_y}{\partial x} + u_y \frac{\partial u_y}{\partial y} = -\frac{\partial p}{\partial y} + \frac{1}{\text{Re}} \left(\frac{\partial^2 u_y}{\partial x^2} + \frac{\partial^2 u_y}{\partial y^2} \right). \quad (3)$$

In equations (1) to (3), u_x and u_y are the dimensionless velocity components along the x -direction and y -direction of a Cartesian coordinate system. Here, p is the pressure.

There are many different lattice Boltzmann methods. For a detailed study of the various LBM methods, the reader is referred to [22, 23]. This section briefly introduces the LBM. The lattice Bhatnagar–Gross–Krook (BGK) model [22] with single-relaxation-time (SRT) is given by [22]

$$f_i(\mathbf{x} + \mathbf{e}_i \delta t, t + \delta t) = f_i(\mathbf{x}, t) + \frac{1}{\tau} (f_i^{(\text{eq})}(\mathbf{x}, t) - f_i(\mathbf{x}, t)). \quad (4)$$

Here, $f_i(\mathbf{x}, t)$, $f_i^{(\text{eq})}(\mathbf{x}, t)$, \mathbf{e}_i , and τ are the particle distribution function at (\mathbf{x}, t) , equilibrium distribution function (the Maxwell–Boltzmann distribution function) at (\mathbf{x}, t) , the particle velocity along the i th direction, and the single-relaxation-time parameter, respectively. Note the two-sides of equation (4) represent the solution. The left hand side applies as a streaming step, and the right hand side gives the collision between the particles. The derivation of Navier–Stokes (N-S) equations from LBM is well known nowadays and can be found in some recently published books (e.g., see [22, 23]). The solution of N-S equations can be calculated iteratively from equation (4).

Collision step:

$$f_i^*(\mathbf{x}, t + \delta t) = f_i(\mathbf{x}, t) + \frac{1}{\tau} (f_i^{(\text{eq})}(\mathbf{x}, t) - f_i(\mathbf{x}, t)), \quad (5a)$$

Streaming step:

$$f_i(\mathbf{x} + \mathbf{e}_i \delta t, t + \delta t) = f_i^*(\mathbf{x}, t + \delta t). \quad (5b)$$

Here, f_i^* represents the postcollision state. One advantage of this is that the streaming step is local in LBM and no need for any computation.

The two-dimensional nine-velocity lattice model ($d2q9$, where d is the dimensions and q is the numbers of particles) [22] is used in this study. In the $d2q9$ (see Figure 1) model, \mathbf{e}_i denotes the nine discrete velocity set, as follows:

$$e_i = 0, \quad \text{for } i = 0,$$

$$e_i = c \left[\cos\left((i-1)\frac{\pi}{4}\right), \sin\left((i-1)\frac{\pi}{4}\right) \right], \quad \text{for } i = 1, 2, 3, 4,$$

$$e_i = c\sqrt{2} \left[\cos\left((i-1)\frac{\pi}{4}\right), \sin\left((i-1)\frac{\pi}{4}\right) \right], \quad \text{for } i = 5, 6, 7, 8. \quad (6)$$

The equilibrium distribution function ($f_i^{(\text{eq})}(\mathbf{x}, t)$) can be solved from

$$f_i^{(\text{eq})} = \rho \omega_i \left[1 + \frac{3}{c^2} (\mathbf{e}_i \cdot \mathbf{u}) + \frac{4.5}{c^4} (\mathbf{e}_i \cdot \mathbf{u})^2 - \frac{1.5}{c^2} (\mathbf{u} \cdot \mathbf{u}) \right]. \quad (7)$$

Here, ω_i is the weighting coefficient. The weighting coefficient, is given by

$$\omega_i = \frac{4}{9}, \quad \text{for } i = 0,$$

$$\omega_i = \frac{1}{9}, \quad \text{for } i = 1, 2, 3, 4, \quad (8)$$

$$\omega_i = \frac{1}{36}, \quad \text{for } i = 5, 6, 7, 8.$$

The density and momentum fluxes in the discretized velocity space can be obtained as

$$\rho = \sum_{i=0}^8 f_i = \sum_{i=0}^8 f_i^{(\text{eq})}, \quad (9)$$

and

$$u = \frac{1}{\rho} \sum_{i=1}^8 f_i = \frac{1}{\rho} \sum_{i=1}^8 f_i^{(\text{eq})}. \quad (10)$$

The pressure can be calculated through the equation of state and is

$$p = \rho c_s^2. \quad (11)$$

The speed of sound for the $d2q9$ model is $c_s = c/\sqrt{3}$ [22]. The corresponding kinematic viscosity in the N-S equations (2) and (3) derived from equation (4) is [22].

$$\nu = (\tau - 0.5)c_s^2 \delta t. \quad (12)$$

It is also known that the single relaxation time LBM is simple and good for parallel systems. Its difficulty lies in the necessity of taking the value of the relaxation time parameter. The stability of the single relaxation time LBM mostly appears at high Reynolds numbers. In such a situation, we need to refine the grids with various relaxation times and to check the results (note that viscosity in lattice units is correlated to the relaxation time). This single relaxation time LBM is conditionally stable and is valid for

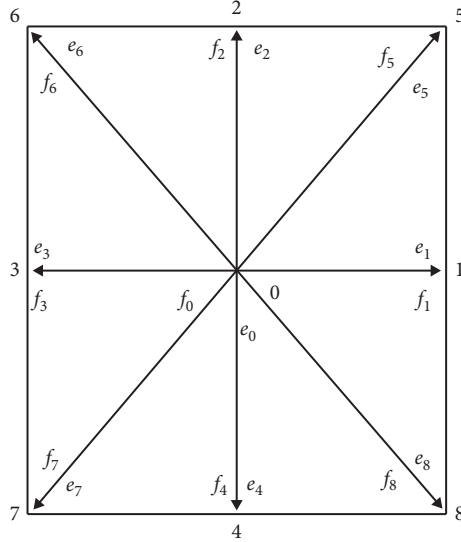


FIGURE 1: A two-dimensional nine-velocity lattice model ((d2q9)).

$\tau > 0.5$. Here, in this problem, the values of τ for $\text{Re} = 100, 150, 200$, and 250 are $0.5263, 0.5175, 0.5132$, and 0.5105 , respectively. One feature of LBM is that the pressure can be calculated through the equation of state instead of Poisson equation [22]. In LBM, we can find the pressure from the equation of state directly once knowing the density instead of using Poisson equation. For the LBM, the CFL (Courant–Friedrichs–Lewy) number is $\text{CFL} = c_s \delta t / \delta x = 1$, which is fixed at unity.

Figure 2 presents the computational domain of flow past a square cylinder in the presence of an upstream attached T-shaped control plate. A square cylinder of size D is placed within the computational domain. A T-shaped control plate of length L is attached to the front surface of the square cylinder. $w = 0.1D$ is the width of the head of the T-shaped control plate. The distance between the left boundary of the domain and the front surface of the T-shaped control plate is $L_u = 10D$, whereas the downstream distance of the domain from the rear surface of the square cylinder to the right boundary of the domain is $L_d = 39D$. The distance between the upper and lower walls is kept as $L_y = 13D$, resulting in a blockage ratio ($\beta = L_y/D = 13$). $L_x = 50D$ is the length of the computational domain. A Cartesian grid was employed, and the origin $(0, 0)$ is set at the center of the main square cylinder. The details of the simulation parameters are summarized in Table 1. C_D and C_L are the drag forces and lift forces in the streamwise and transverse directions, respectively.

The following boundary conditions are incorporated in the present study.

- (i) At inlet, uniform inflow velocity is applied, $u = 0.04385, v = 0$
- (ii) At outlet, convective boundary condition is applied [24]

- (iii) At the upper and lower walls of the domain, no-slip ($u = v = 0$) is applied
- (iv) At the square cylinder and T-shaped control plate surfaces, no-slip boundary condition is imposed

The forces acting on the surfaces of the square cylinder can be calculated from the momentum-exchange method [25].

The implementation of the LBM is simple and straightforward. The following steps are presented for calculating forces and fluid properties:

- (i) Specify the streaming time step δt . Calculate the single relaxation time parameter τ
- (ii) The local distribution function must be updated through collision step (equation (5a))
- (iii) The fluid particles are streamed to neighboring streaming lattice nodes through the streaming step (equation (5b))
- (iv) Implement suitable initial and boundary conditions for the distribution function
- (v) Calculate macroscopic variables (equations (9) and (10))
- (vi) Repeat steps (ii) to (iv) until the convergence criteria or the assigned maximum iteration numbers are reached

It is noticed that the lattice Boltzmann equation only requires the streaming step and collision step to evolve the fluid filled with complex nonlinearities. No special treatment is required for nonlinear terms in Navier–Stokes equations. The LBM explicitly calculates the pressure from the density. For computations, the simulation parameters are shown in Table 1.

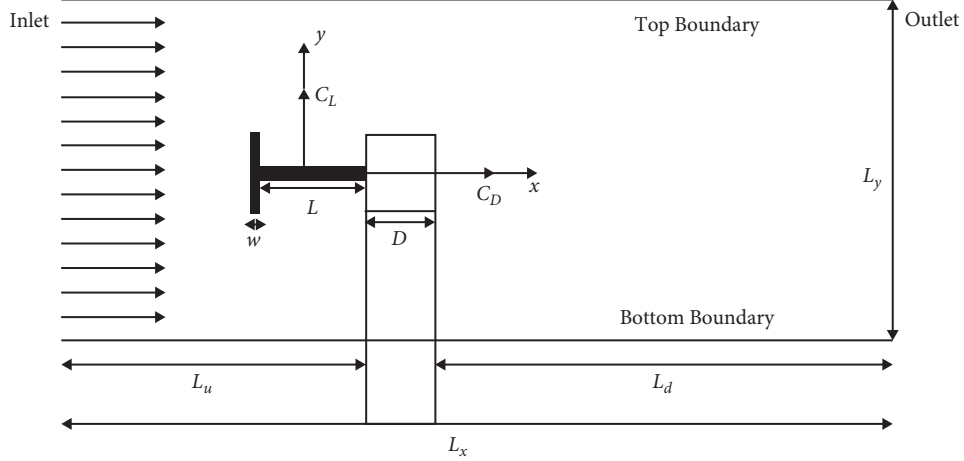


FIGURE 2: Schematic diagram of the proposed problem.

TABLE 1: Simulation parameters.

Re	U_∞	τ
100	0.04386	0.5263
150	0.04386	0.5175
200	0.04386	0.5132
250	0.04386	0.5105

The vorticity (dimensional) is defined as

$$\omega_z = \frac{\partial v}{\partial x} - \frac{\partial u}{\partial y}. \quad (13)$$

Here, u and v are the velocity components in the streamwise direction and transverse direction, respectively. It is to be noted that the vorticity is calculated by using a second-order central difference scheme and is then non-dimensionalized by the uniform inflow velocity (U_∞) and the side length of the square cylinder (D):

$$\phi_z = \frac{D\omega_z}{U_\infty^2}. \quad (14)$$

For analysis, we have defined the following nondimensional parameters as given in equations (15)–(18)

$$Re = \frac{U_\infty D}{U}, \quad (15)$$

$$C_D = \frac{F_x}{0.5} \rho U_\infty^2 D, \quad (16)$$

$$C_L = \frac{F_y}{0.5} \rho U_\infty^2 D, \quad (17)$$

$$St = \frac{f_s D}{U_\infty}. \quad (18)$$

Here, Re , C_D , C_L , and St are the Reynolds number, drag coefficient, lift coefficient, and Strouhal number, respectively. It is to be noted here, F_x and F_y are the drag and lift forces experienced by the square cylinder along with the streamwise and transverse directions, respectively. These

forces are calculated using the momentum-exchange method [25]. f_s is the vortex shedding frequency calculated using the fast Fourier transformation (FFT) of the time series of the lift coefficient, C_L .

The stopping criteria once we get the steady state is

$$\frac{\sum_{ij} |u_{ij}^{(n+1)} - u_{ij}^n|}{\sum_{ij} |u_{ij}^{(n+1)}|} \leq 1 \times 10^{-6}. \quad (19)$$

It is noticed that $U_\infty = \delta x / \delta t U_{lb}$ represents the velocity in a system of lattice units. Here, U_{lb} represents the lattice Boltzmann velocity. In LBM, U_{lb} is proportional to the Mach number of the fluid. In Tables 2–5, the percentage deviation is also given in brackets. For $D = 10, 20, 30$, and 40 , the mean drag coefficient (C_{Dmean}), Strouhal number (St), root-mean-square value of drag coefficient (C_{Drms}), and lift coefficient (C_{Lrms}) values are as shown in Table 2. Here, $D (= \delta x)$ represents the lattice units on each side of the square cylinder and T-shaped control plate. The numerical results for C_{Dmean} , St , C_{Drms} , and C_{Lrms} in Tables 3–5 for different values of blockage ratio ($\beta = L_y/D$), L_u , and L_d , respectively. The results presented in Tables 2–5 have been performed at $Re = 250$ and $L/D = 5$. Inspection of Table 2 shows, however, that the D effect dies away as $D \geq 20$. Guo et al. [24] proposed and used that $D = 20$ is reasonably good to achieve good numerical results for the square cylinder. The blockage ratio β is 7.7%. It is observed that the β -value beyond 13 does not have any considerable influence on the integral parameters presented in Table 3. It was previously expressed that a good two-dimensional result can be achieved for flow of a square cylinder with a blockage ratio greater than about 5% [39]. One can also see the effect of L_u and L_d in Tables 4 and 5, respectively. In the present numerical study, the value of the blockage ratio is already more than 5%. $D = 20$, $\beta = 13$, $L_u = 10D$, and $L_d = 39D$ is, therefore, used for all computations in the present numerical study.

In order to ensure the validity of the code, we calculate the integral parameter values for $Re = 100, 150, 200$, and 250 for comparison with available data for flow past a square cylinder without T-shaped control plate. A comparison of

TABLE 2: Effect of different grids points for $\text{Re} = 250$, $L/D = 5$, $\beta = 13$, $L_u = 10D$, and $L_d = 39D$.

D	C_{Dmean}	St	C_{Drms}	C_{Lrms}
10	-0.2985 (5.0%)	0.1135 (4.6%)	0.0359 (4.7%)	0.3156 (4.1%)
20	-0.2846	0.1083	0.0342	0.3028
30	-0.2804 (1.5%)	0.1072 (1.0%)	0.0336 (1.8%)	0.2987 (1.4%)
40	-0.2812 (1.2%)	0.1072 (1.0%)	0.0337 (1.5%)	0.2995 (1.1%)

TABLE 3: Influence of β for $\text{Re} = 250$, $L/D = 5$, $L_u = 10D$, and $L_d = 39D$.

β	C_{Dmean}	St	C_{Drms}	C_{Lrms}
6	-0.2972 (4.4%)	0.1132 (4.3%)	0.0356 (4.0%)	0.3152 (4.0%)
13	-0.2846	0.1083	0.0342	0.3028
18	-0.2832 (0.5%)	0.1075 (0.7%)	0.0338 (1.2%)	0.3004 (0.8%)

TABLE 4: Influence of L_u for $\text{Re} = 250$, $L/D = 5$, $\beta = 13$, and $L_d = 39D$.

L_u	C_{Dmean}	St	C_{Drms}	C_{Lrms}
5	-0.2698 (5.5%)	0.1148 (5.7%)	0.0359 (4.7%)	0.3192 (5.1%)
10	-0.2846	0.1083	0.0342	0.3028
15	-0.2798 (1.7%)	0.1066 (1.6%)	0.0337 (1.5%)	0.2987 (1.4%)
20	-0.2803 (1.5%)	0.1066 (1.6%)	0.0338 (1.2%)	0.2998 (1.0%)

TABLE 5: Influence of L_d for $\text{Re} = 250$, $L/D = 5$, $\beta = 13$, and $L_u = 10D$.

L_d	C_{Dmean}	St	C_{Drms}	C_{Lrms}
15	-0.2739 (4.0%)	0.1132 (4.3%)	0.0356 (4.0%)	0.3165 (4.3%)
25	-0.2846	0.1083	0.0342	0.3028
35	-0.2802 (1.4%)	0.1069 (1.3%)	0.0337 (1.5%)	0.2987 (1.4%)
45	-0.2814 (1.1%)	0.1069 (1.3%)	0.0339 (0.9%)	0.3001 (0.9%)

the present results with the available data is given in Table 6. Our numerical results are generally in good agreement with available published data. The present results almost fell within the range of available numerical values, even some experimental values (Okajima [27], Norberg [28]). There are some slight differences between the present and experimental results. Their differences arise from experimental uncertainties, using various boundary conditions, the effect of blockage, grid structures, etc.

3. Results and Discussion

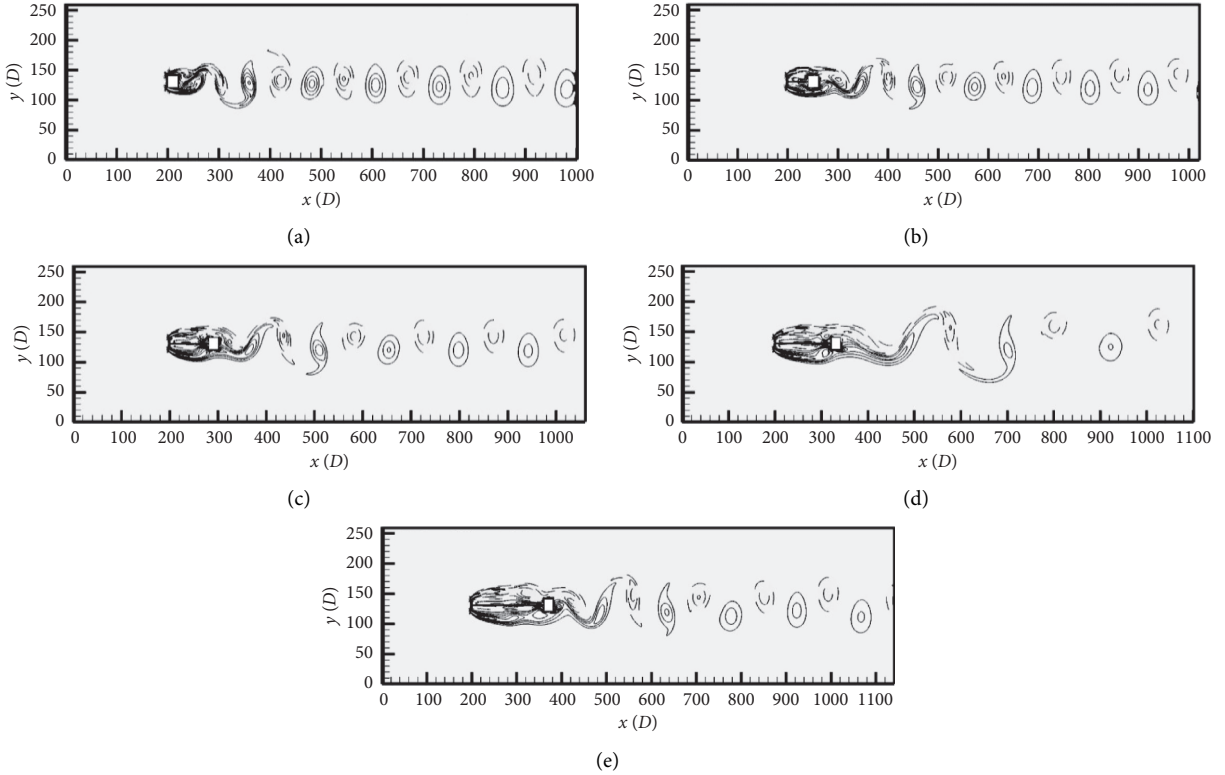
It is clear from previous investigations that the reduction of fluid forces and wake control depend on active and passive techniques. Keeping in view these importance, the present study was conducted to systematically analyze the importance of upstream attached T-shaped control plate length, ranging from $L/D = 0.5$ to 8 at Reynolds numbers, $\text{Re} = 100$, 150, 200, and 250. The present numerical results are calculated after the dynamic steady-state condition is reached (see equation (19)). The most important findings on the basis of our numerical investigation will be presented in this section in detail.

Figures 3(a)–3(e) presents the vorticity contours visualization around the square cylinder with and without a T-shaped control plate. Five different cases, one is without

T-shaped control plate ($L/D = 0$) and another four cases with different T-shaped control plate lengths ($L/D = 2, 4, 6, 8$) are considered for the various flow pattern investigation. The solid and dotted lines represent the positive and negative vortices, respectively. It can be seen from the figure that there is no vortex shedding from the T-shaped control plate at any length due to its attachment with the main square cylinder. Strouhal number (St) of the isolated cylinder and the square cylinder with upstream attached T-shaped control plate at lengths of 2, 4, 6, and 8 are 0.1510, 0.1618, 0.1316, 0.0896, and 0.1316, respectively. It is observed from the St values that the length of the T-shaped control plate caused a decrease and increase in the vortex shedding frequency of the main square cylinder. This decrease and increase can be further confirmed from the vorticity graphs. Qualitatively, the number of vortices that appeared behind the main square cylinder decreased from 13 to 10 for $L/D = 2$ and 4, to 6 for $L/D = 6$ and then increased from 6 to 11 for $L/D = 6$ and 8. It is observed that the formation of vortices is quite sensitive to the length of the upstream attached T-shaped control plate. From these figures, we can draw some important conclusions about flow characteristics. For all L/D values in Figures 3(a)–3(e), the alternate generation of shed vortices can be clearly seen behind the main square cylinder. This flow is called the single bluff-body flow regime. Shed vortices travel in alternate fashion throughout the flow field. We further divided the single bluff-

TABLE 6: Comparison of present results of flow past a square cylinder with available results.

$Re = 100$	C_{Dmean}	St	C_{Drms}	C_{Lrms}
Present	1.4125	0.1450	0.0035	0.1780
Dash et al. [6] (num)	1.460	0.1440	...	0.1840
Luo et al. [26] (exp)	...	0.142–0.145
Okajima [27] (exp)	...	0.140
Norberg [28] (exp)	...	0.140
Sohankar et al. [29] (num)	1.444	0.1450	0.0019	0.130
Saha et al. [30] (num)	0.0030	0.122
$Re = 150$	C_{Dmean}	St	C_{Drms}	C_{Lrms}
Present	1.4012	0.1520	0.0172	0.2732
Okajima [27] (exp)	...	0.1420
Norberg [28] (exp)	...	0.1550
Sohankar et al. [29] (num)	1.4080	0.1610	0.0061	0.1770
Saha et al. [30] (num)	0.0170	0.2740
$Re = 200$	C_{Dmean}	St	C_{Drms}	C_{Lrms}
Present	1.4268	0.1510	0.0294	0.3250
Okajima [27] (exp)	...	0.1440
Norberg [28] (exp)	...	0.1520
Sohankar et al. [29] (num)	1.424	0.165	0.0121	0.240
Saha et al. [30] (num)	0.0260	0.305
Dutta et al. [31] (exp)	1.410	0.154
$Re = 250$	C_{Dmean}	St	C_{Drms}	C_{Lrms}
Present	1.4432	0.1482	0.0348	0.4050
Sohankar et al. [29] (num)	1.4490	0.1510	0.0162	0.375
Saha et al. [30] (num)	0.0320	0.150

FIGURE 3: Instantaneous vorticity contours visualization of square cylinder in presence of attached T-shaped control plate at $Re = 200$. (a) Square cylinder without T-shaped control plate. (b) $L/D = 2$. (c) $L/D = 4$. (d) $L/D = 6$. (e) $L/D = 8$.

body flow regime into two different flow regimes. One is called the single bluff body with primary vortex shedding frequency (regime-I), and the second one is called the single

bluff body with secondary frequencies together with primary vortex shedding frequency (regime-II). In the case of regime-I, one can see only one dominant shedding frequency peak in

the power spectra (see Figures 4(a) and 4(b)). While in the case of regime-II, one can see some minor extra peaks called secondary frequencies together with the dominant vortex shedding frequency (Figures 4(c) and 4(d)). It can also be seen from Figures 3(b)–3(e), the generated shear layers from the bottom and top side of the head of the T-shaped control plate attach to the front and bottom and top sides of the main square cylinder, and then, they combined with the generated shed vortices from the main square cylinder.

Figures 5(a)–5(e) shows the instantaneous streamlines at different T-shaped control plate lengths at $Re = 200$. It is observed that the T-shaped control plate length will affect flow features, especially in the wake region.

At $L/D = 0$ (Figure 5(a)) where it is the single bluff body flow pattern, one bigger eddy is located behind the rear surface of the square cylinder without T-shaped control plate. In Figure 5(b) as $L/D = 2$, there is a small eddy at the bottom of the main square cylinder. The streamline graph further confirms that the shear layers separated from the top and bottom surfaces of the head of the control plate directly reattach to the main square cylinder. Some waviness was also observed in the wake region for all cases presented in Figures 5(a)–5(e). It is clear from Figure 5(c) that there is no close recirculation zone behind the main square cylinder. The streamline graphs further confirm that the separation point changes due to T-shaped attached control plate as compared to the square cylinder (without T-shaped control plate).

Figures 6(a)–6(e) shows the instantaneous pressure contours at different T-shaped control plate length at $Re = 200$. The use of an upstream attached T-shaped control plate, irrespective of what the flow regime is, reduces the pressure difference between the front surface of the T-shaped control plate and the rear surface of the main square cylinder. As a result, a reduction of the mean drag coefficient in comparison with an isolated occurs. Furthermore, as the L/D value increases, the pressure distribution above and below the length of the T-shaped control plate also changes.

As we have seen from the vorticity contours and streamlines that flow changes its characteristics from single bluff body to steady flow and then from steady flow to unsteady flow by changing the values of L/D . This can also be analyzed from Figures 7(a) and 7(b) which presents the time histories of C_D and C_L at various values of L/D and shows that the amplitude of forces changed by varying L/D values. It is seen from Figure 6(a) that the C_D variation is very sensitive to the T-shaped control plate length. The variation of C_D for $L/D = 4, 6$, and 8 are more sensitive than that for $L/D = 2$. The oscillations amplitude for the C_L in comparison with an isolated cylinder (without T-shaped control plate) decreases.

The power spectrum of lift coefficients at $L/D = 2, 4, 6$, and 8 are shown in Figures 4(a)–4(d). The highest peak in the graphs refers to the primary vortex shedding frequency (St_p), and the other small peaks represent the secondary frequencies (St_s). In the power spectra graph, 'E' stands for energy. The single dominant peak confirms the periodic nature of lift coefficients at $L/D = 2$ and 4 (Figure 6(b)). Some

small modulation exists for $L/D = 6$ and 8 in lift coefficients, and as a result, one can see one or two extra small peaks together with the primary vortex shedding frequency.

The instantaneous vorticity contours visualization shown in Figures 8(a)–8(d) clearly illustrates the influence of Re on the flow characteristics. It should be noted that, in the case $L/D = 5$ at $Re = 100$, we observed complete suppression of vortex shedding. This flow regime is called the steady flow regime (regime-III). In steady flow regime only, the streamline can be seen behind the cylinder without any recirculation or shed vortices. These figures clearly illustrate the basic difference between steady flow and single bluff-body flow. Flow behind the main square cylinder, identified by Karman vortex street at $Re = 150$, has almost similar vortices in alternating fashion from upper and lower surface of the main square cylinder (Figure 8(b)). This flow is called regime-I. In addition, as Reynolds number increased, we observed regime-II. Figures 8(c) and 8(d) show that periodic vortex shedding is further maintained when we increased the Reynolds number Re to 250. As Re increases above 100, the number of shed vortices increases, and consequently, the drag force decreases; see Figure 9(a). It is also noted that the vortices are shed alternatively, and the sizes of the shed vortices from the top and bottom surfaces of the main square cylinder are different. The latter tends to elongate in the near wake, and the former is almost round. This is because of the upstream attached T-shaped control plate length and increased Reynolds numbers. Furthermore, its strength increases as the value of Re increases. As a result, the Strouhal numbers of the square cylinder with the upstream attached T-shaped control plate at Reynolds numbers of 150, 200, and 250 are 0.1024, 0.1056, and 0.1104, respectively.

Figures 10(a)–10(d) show the pressure distributions along the front and back sides of the main square cylinder with different Reynolds numbers at $L/D = 5$. As shown, the pressure distribution on the back side for all Reynolds numbers is considerably changed; thus, the remarkable differences in drag forces are mainly due to the differences in the pressure distribution along the surfaces of the length of the T-shaped control plate. It is observed that the maximum value of pressure exists at the center point of the front surface. However, as the value of Re changes, the pressure distribution on the surfaces of the length of the control plate changes considerably.

The graphical representation of C_D and C_L shown in Figures 9(a) and 9(b) further indicate the flow transitions. The lift coefficient represents the transverse force component which represents the magnitude of the vortex shedding, since no vortices shed from the main square cylinder; that is why, the lift force is steady for $Re = 100$ at $L/D = 5$. It is noticed that due to the steady flow nature the straight constant line can be clearly seen for C_D and C_L in Figures 9(a) and 9(b). The profiles of C_L confirm the periodic nature of the flow except for the C_D at $Re = 150, 200$, and 250 . The periodic nature confirms that the vortices shed from the upper and lower sides of the cylinder with the same frequency. It is also observed that the C_L amplitude is somewhat increased as the value of Re increased. The negative drag

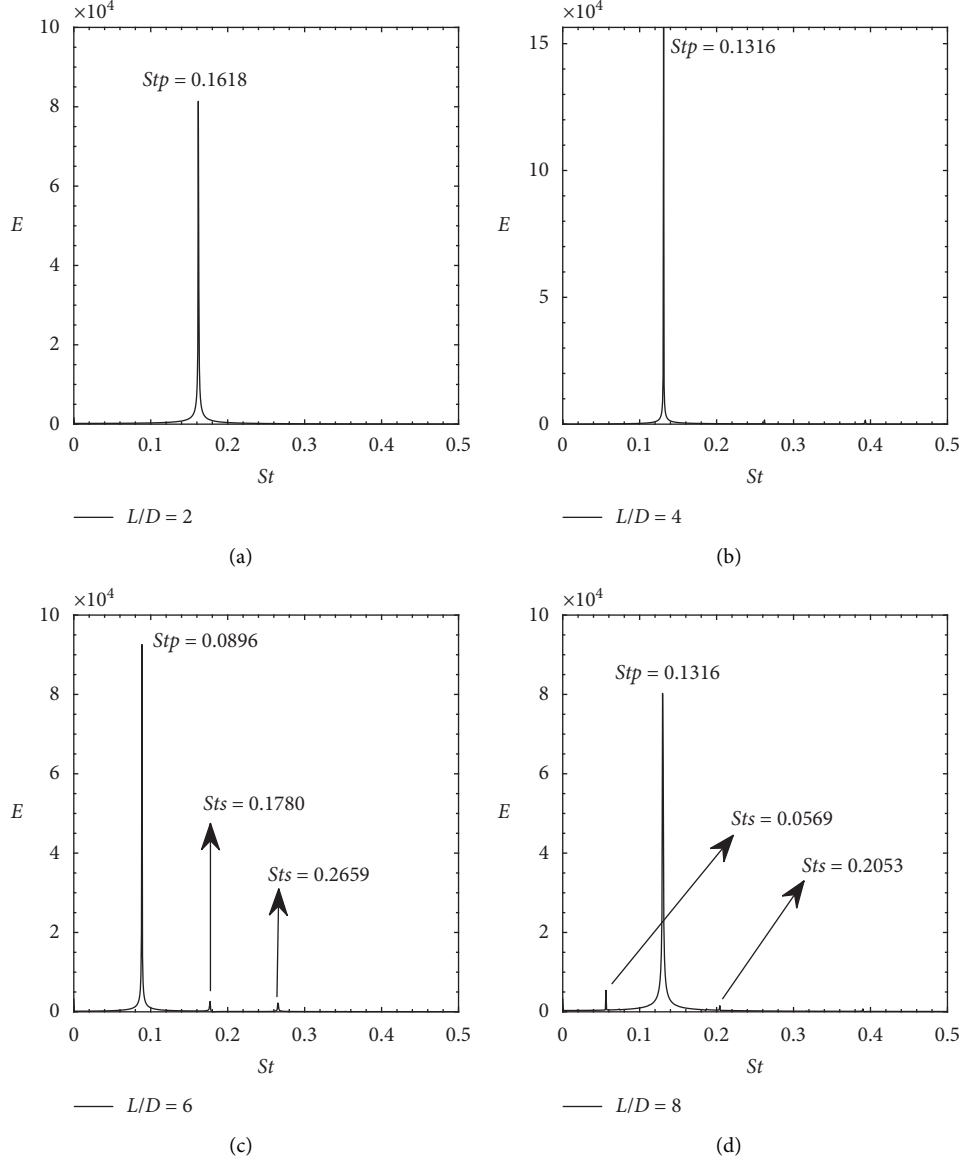


FIGURE 4: Power spectra analysis of fluctuating lift coefficient at $Re = 200$ for different T-shaped control plate length: (a) $L/D = 2$, (b) $L/D = 4$, (c) $L/D = 6$, and (d) $L/D = 8$.

value is observed for $Re = 150$, 200 , and 250 . Due to the presence of T-shaped control plate no periodic nature is observed for $Re = 150$, 200 , and 250 .

Figures 11(a)–11(c) shows the spectra analysis of the fluctuating lift coefficient at $L/D = 5$ for different Reynolds numbers. It is to be noted that due to the constant nature of C_L for $Re = 100$, no vortex shedding is observed behind the cylinder. The power spectra show two minor peaks together with the dominant vortex shedding frequency in the case of regime-II. But still, the primary vortex shedding frequency is the dominant frequency. The dominant primary vortex shedding frequency peak is seen in all the chosen cases presented in Figures 11(a)–11(c), which confirms the single frequency observed in the time trace analysis of lift coefficient C_L .

The instantaneous vorticity contour visualization shown in Figures 12(a)–12(e) clearly illustrates the influence of L/D

on the flow characteristics. It is clear from Figures 12(a)–12(d) that the vortices are shed alternatively from the upper and lower surfaces of the main square cylinder. The spacing between the two shed vortices is almost constant. However, the size of the vortex shed from the upper side of the square cylinder is comparatively larger than the size of the vortex shed from the lower side of the square cylinder. This may be due to the length of the T-shaped control plate, but still alternating vortex shedding can be clearly seen behind the square cylinder. The T-shaped control plate length effect can be seen more clearly from streamlines in Figure 12(e) for $L/D = 6$. In Figure 12(e), the flow is completely suppressed, and no alternate vortex shedding can be seen behind the square cylinder. This is called the steady flow regime (regime-III). It is also seen that the vortex formation length becomes longer, and the transverse spacing

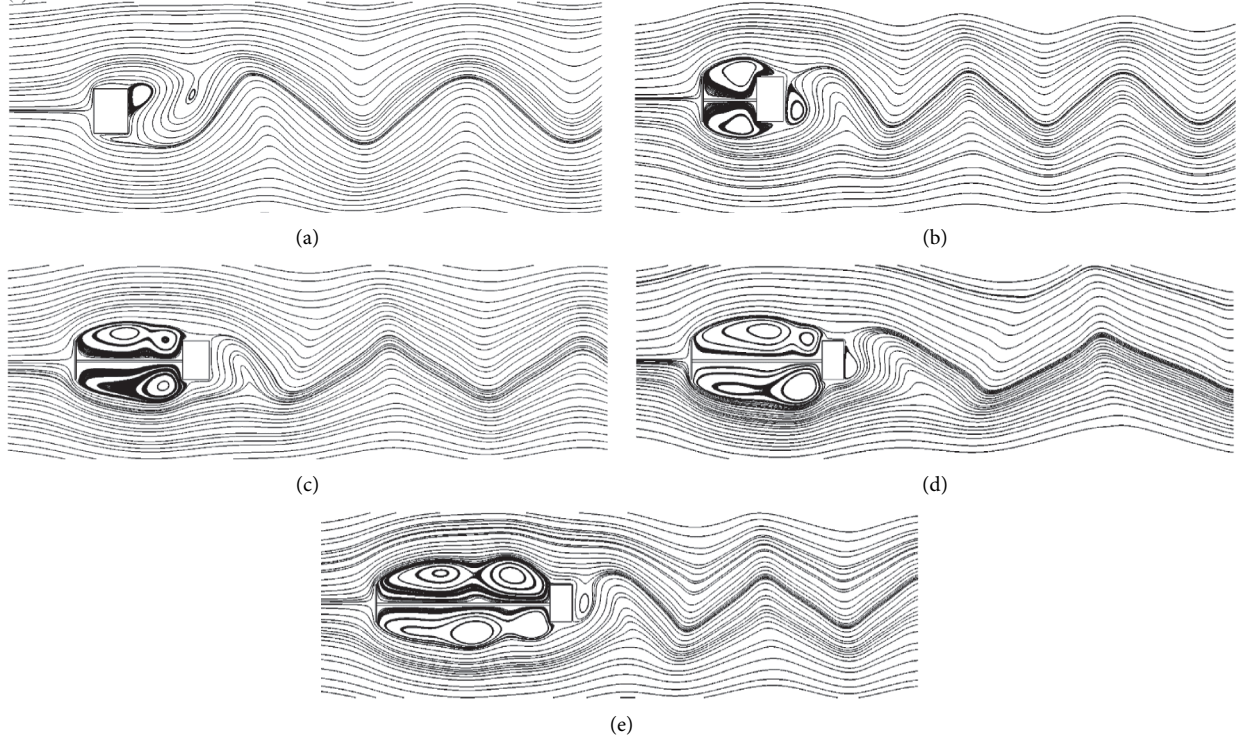


FIGURE 5: Comparison of the streamlines in the near wake of the main square cylinder with and without an upstream T-shaped control plate at at $\text{Re} = 200$: (a) square cylinder without T-shaped control plate, (b) $L/D = 2$, (c) $L/D = 4$, (d) $L/D = 6$, and (e) $L/D = 8$.

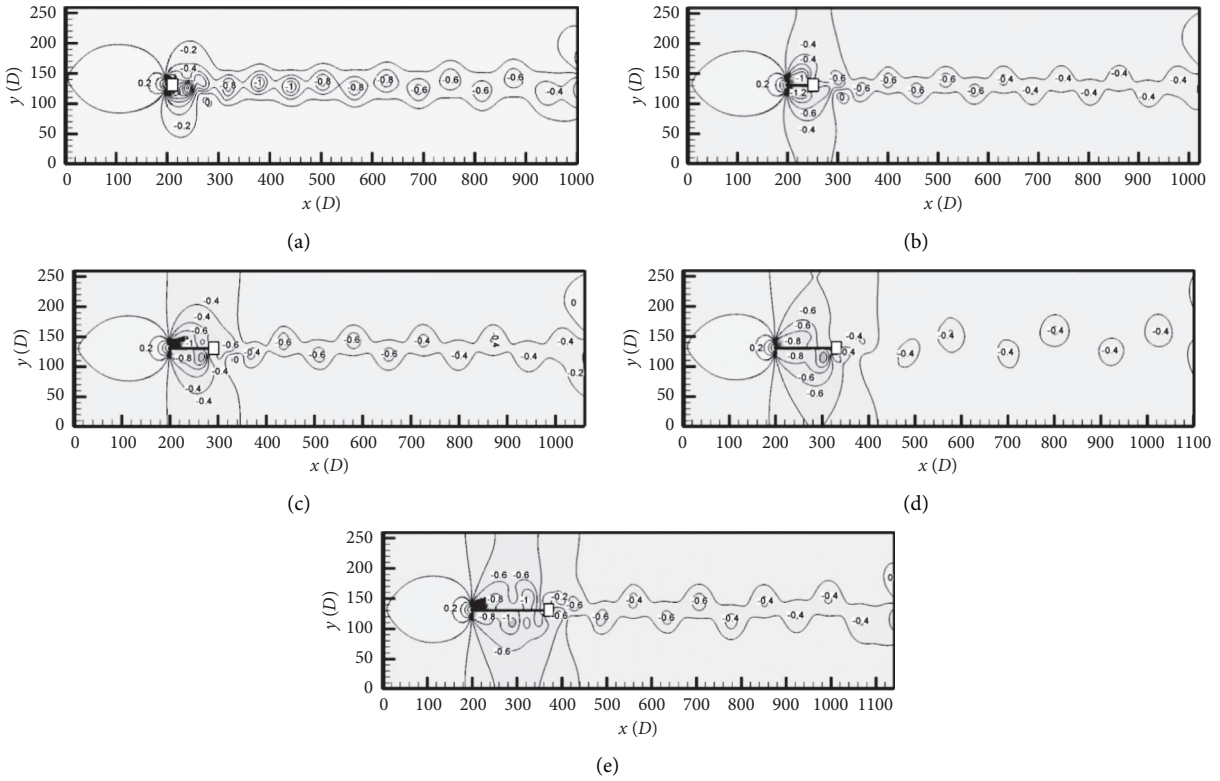


FIGURE 6: Pressure contours visualization of square cylinder in presence of attached T-shaped control plate at $\text{Re} = 200$: (a) square cylinder without T-shaped control plate, (b) $L/D = 2$, (c) $L/D = 4$, (d) $L/D = 6$, and (e) $L/D = 8$.

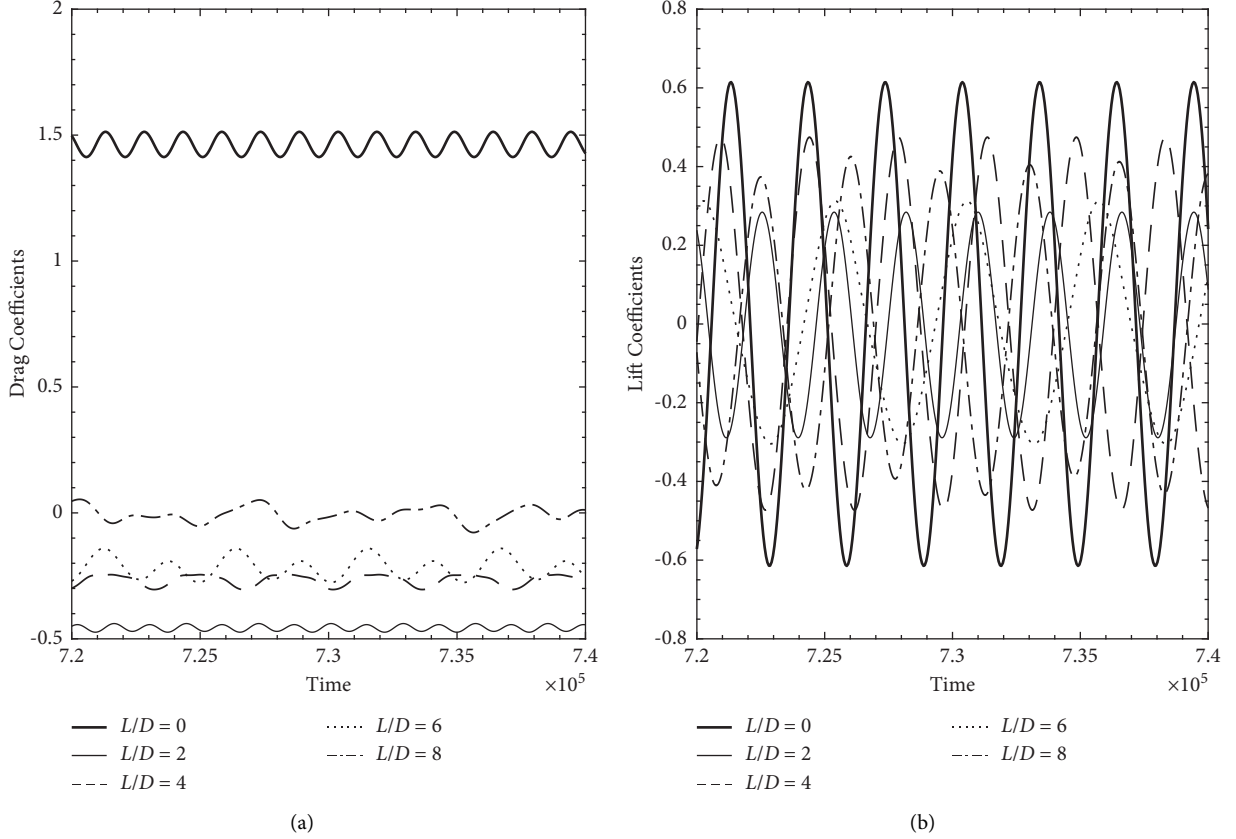


FIGURE 7: Time histories of (a) drag coefficients and (b) lift coefficients of square cylinder at $Re = 200$ for different T-shaped control plate length.

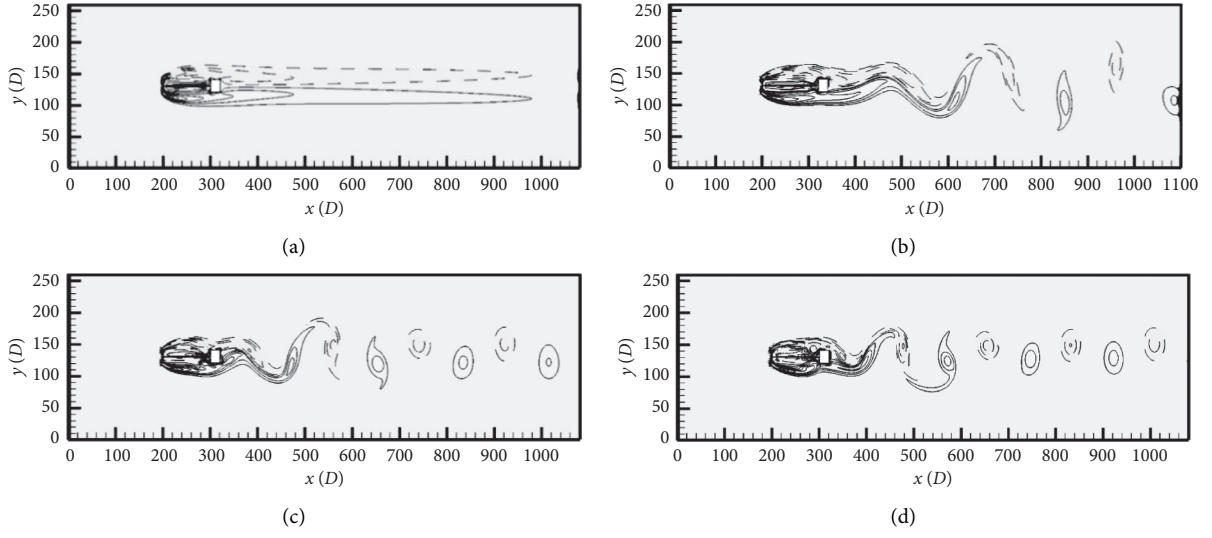


FIGURE 8: Instantaneous vorticity contours visualization at $L/D = 5$: (a) $Re = 100$, (b) $Re = 150$, (c) $Re = 200$, and (d) $Re = 250$.

between the shed vortices becomes smaller as the value of L/D increased from 0 to 4. Such observations were found by Zhou et al. [32] for flow past a circular cylinder using tripping rods at angles (θ) = 40° and $Re = 200$. This confirms that the T-shaped control plate can also be used to understand the flow characteristics behind the bluff body.

As we have seen from the vorticity contours and streamlines that flow changes its characteristics from single bluff body to steady flow regime by changing the values of L/D . This can also be analyzed from Figures 13(a) and 13(b) which present the time histories of C_D and C_L at various values of L/D and show that the amplitude of forces changed by varying L/D

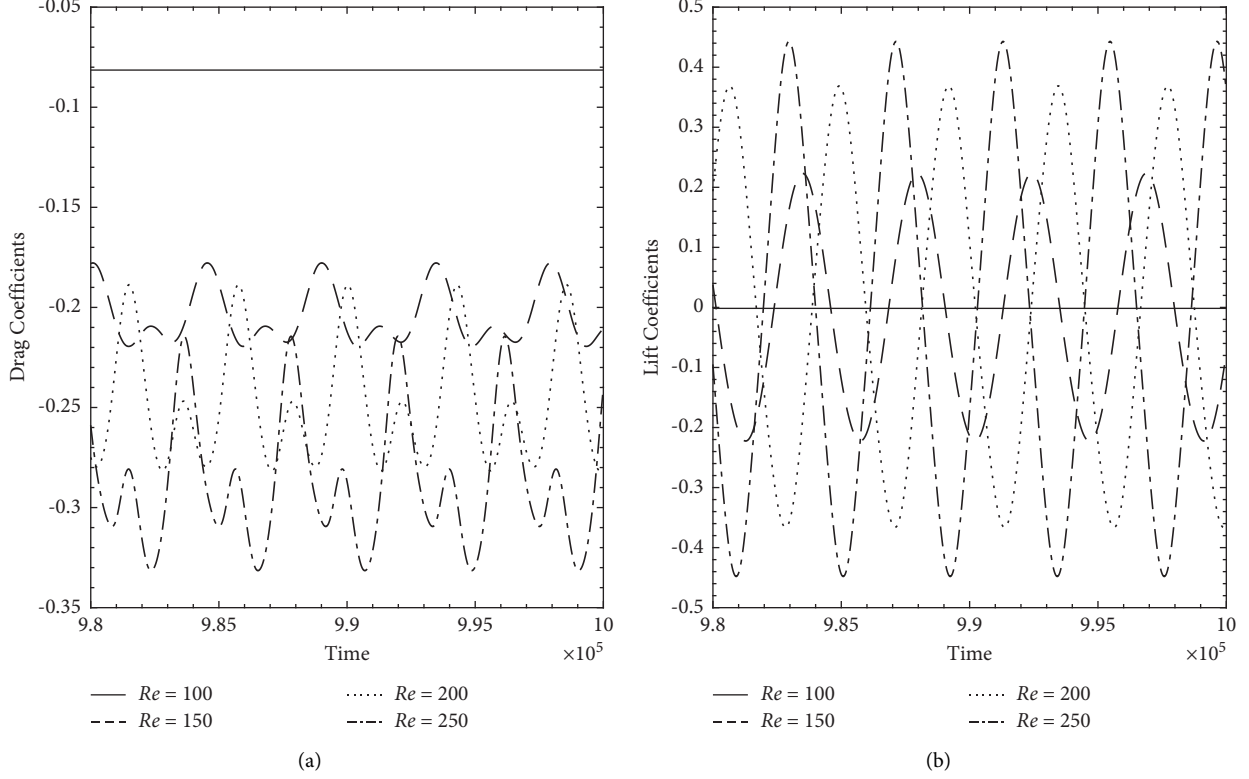


FIGURE 9: Time histories of (a) C_D and (b) C_L of square cylinder at $L/D = 5$ for different Reynolds numbers.

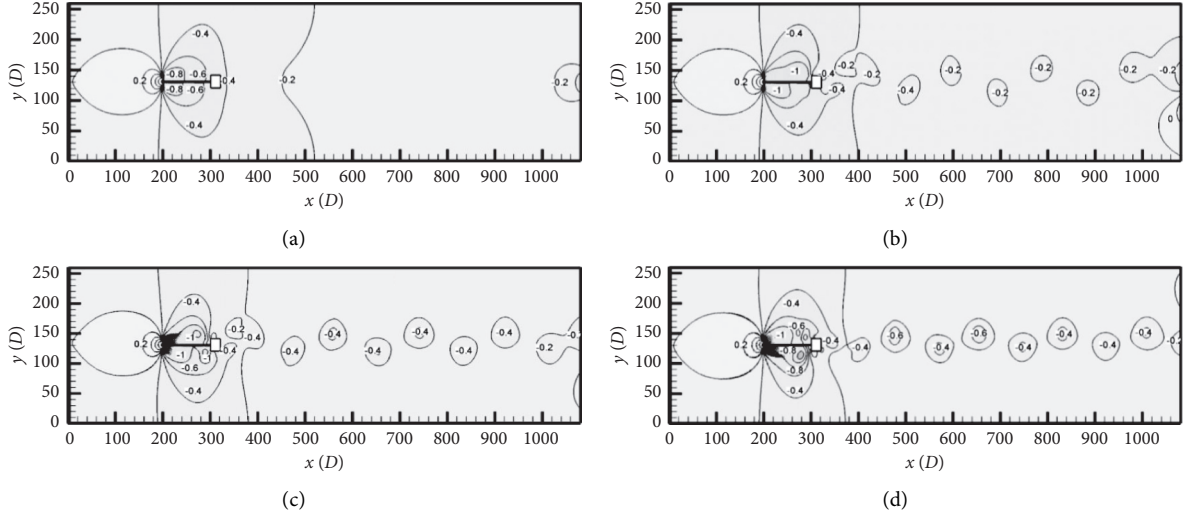


FIGURE 10: Pressure contours visualization at $L/D = 5$: (a) $Re = 100$, (b) $Re = 150$, (c) $Re = 200$, and (d) $Re = 250$.

values. The lift coefficient of $L/D = 1, 2$, and 4 has periodic nature with smaller amplitude cycle compared to those observed for flow past an isolated cylinder ($L/D = 0$) in Figure 13(b). At $L/D = 6$, the constant behavior can be observed for the square cylinder. The periodic nature of C_L confirms the alternate shedding behaviour from cylinder at $L/D = 0, 1, 2$, and 4 . The periodic nature of C_L shows the periodic nature of the flow with almost constant amplitude. This periodic nature confirms that the vortices shed from the upper

and lower surface of the main square cylinder with same frequency. One can also observe that the C_L amplitude is somewhat increased in the case of $L/D = 2$ than $L/D = 4$.

The forces acting on the square cylinder in the streamwise and transverse directions by the fluid are the important criteria to analyze the flow characteristics quantitatively, and thus, the $C_{D\text{mean}}$, St , C_{Drms} , and C_{Lrms} are depicted in Figures 14(a)–14(h), respectively, where the solid and dotted straight lines refer to the case of a square cylinder

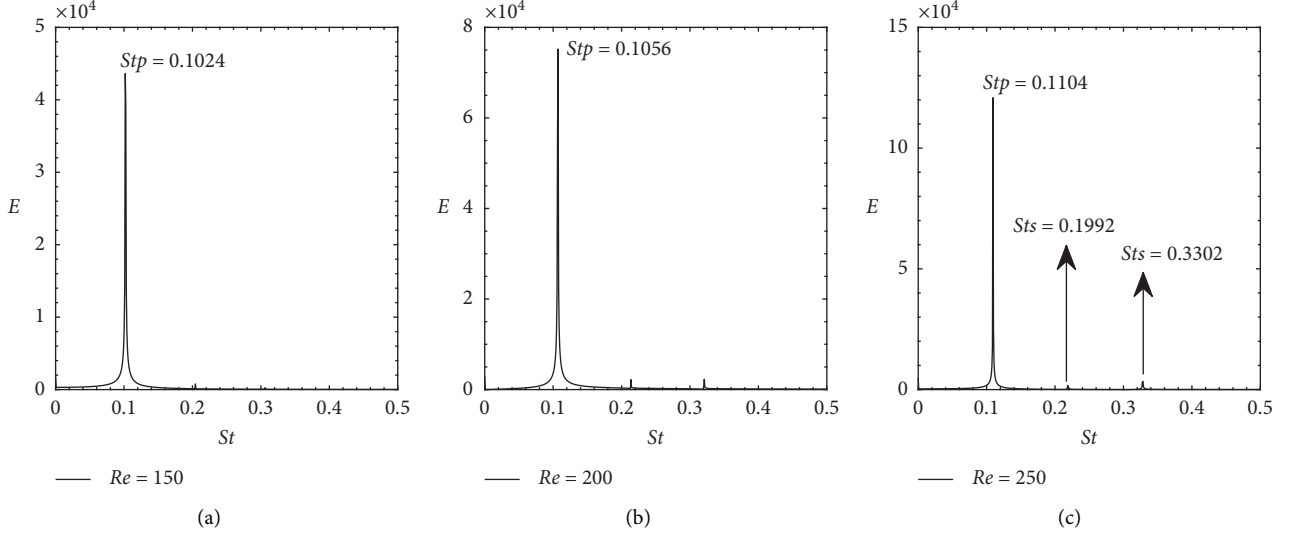


FIGURE 11: Spectra analysis of C_L using the FFT at $L/D = 5$ for various Reynolds numbers: (a) $Re = 150$, (b) $Re = 200$, and (c) $Re = 250$.

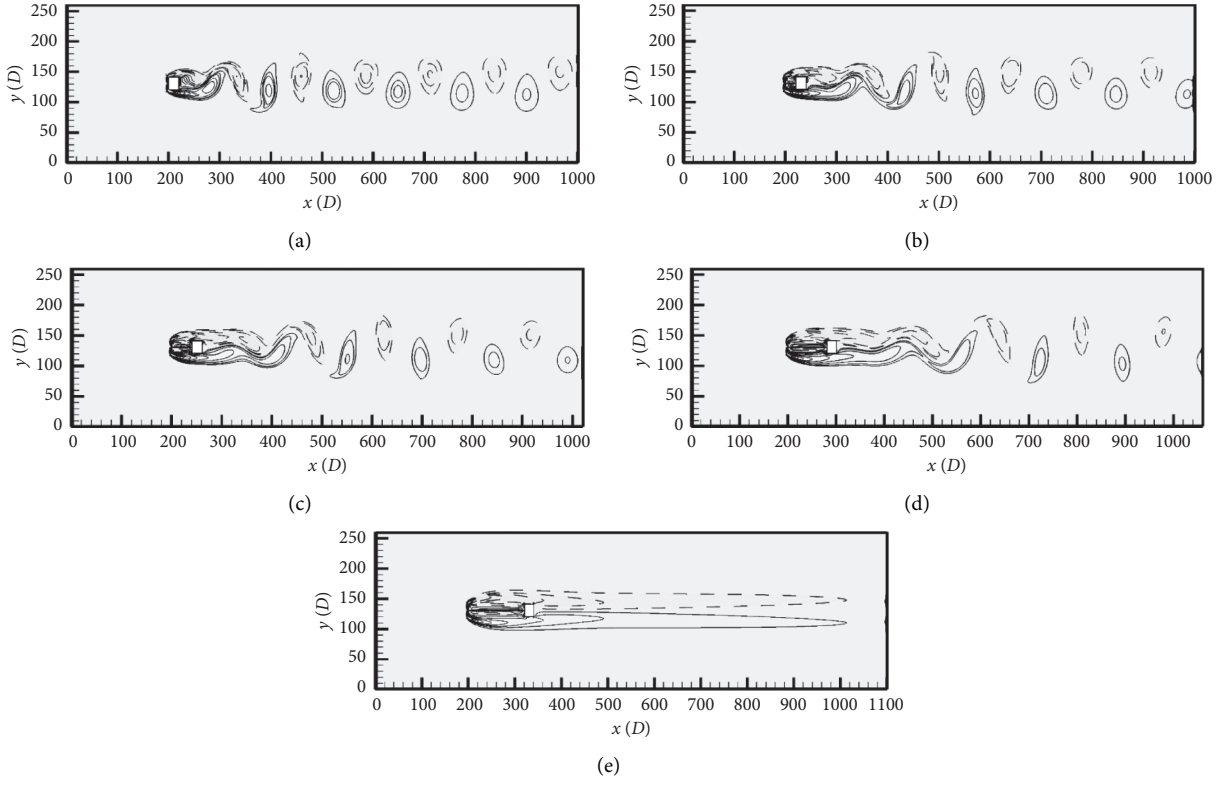


FIGURE 12: Instantaneous vorticity contours visualization at $Re = 100$: (a) $L/D = 0$, (b) $L/D = 1$, (c) $L/D = 2$, (d) $L/D = 4$, and (e) $L/D = 6$.

without the T-shaped control plate. It is seen from Figures 14(a) and 14(b) that C_{Dmean} of the square cylinder with T-shaped control plate is lower than that of an isolated cylinder without the T-shaped control plate ($L/D = 0$) for all considered Reynolds numbers. It is seen that the C_{Dmean} slightly increases with increasing Re . A maximum value of 0.1538 of C_{Dmean} is observed for $(L/D, Re) = (8, 200)$ and a

minimum value of -0.520 of C_{Dmean} is noticed for $(L/D, Re) = (0.5, 150)$. As the vortex length increases with narrow wake, the pressure on the rear surface of the square cylinder increases, and as a result, the drag reduces.

It is noticed that the St number decreases with the increase in L/D and experiences sudden jump at $L/D = 7$ at $Re = 100, 150$, and 200 , which confirms the changes in flow

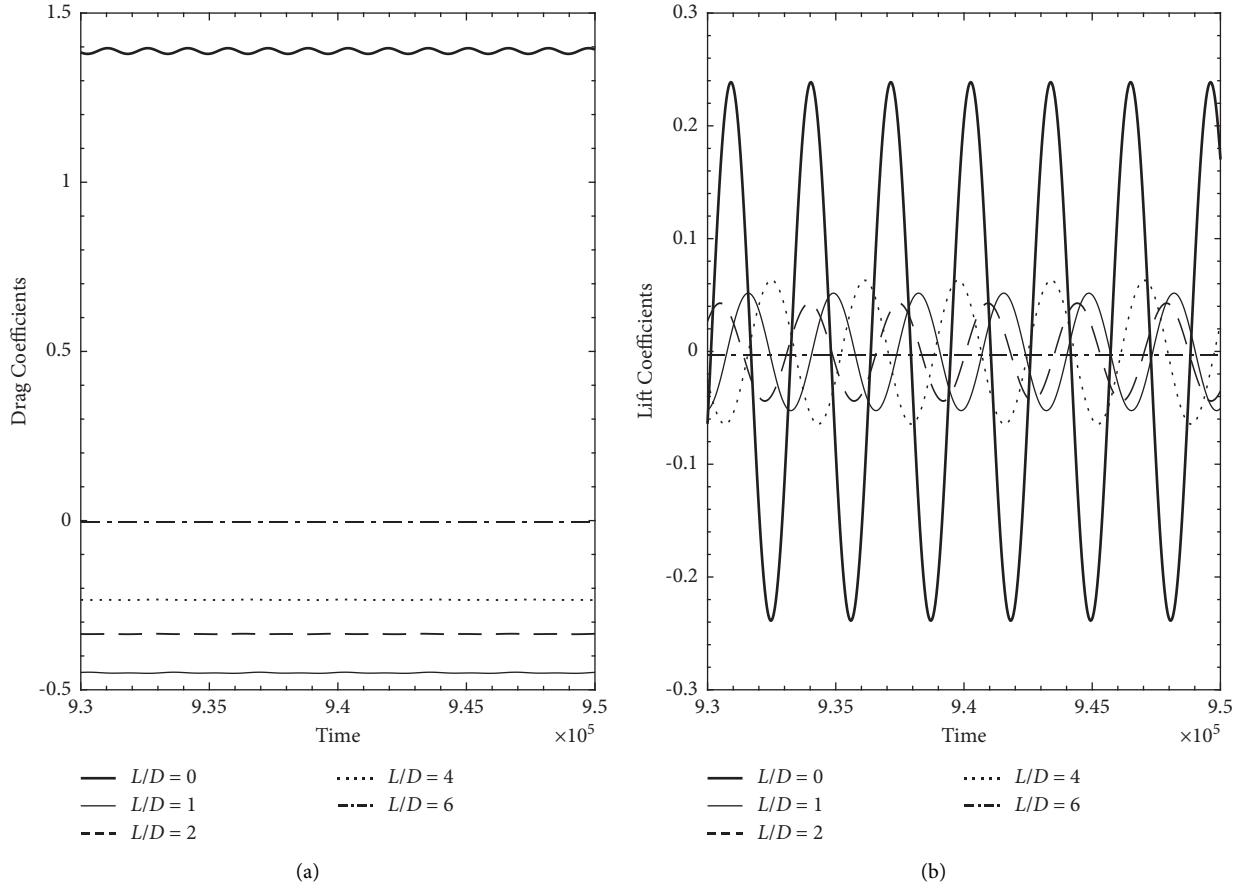


FIGURE 13: Time histories of (a) drag coefficients and (b) lift coefficients of square cylinder at $Re = 100$ for different T-shaped control plate length.

characteristics. The value of St for $L/D \geq 2.5$ exceeds the value of the single cylinder for $Re = 150, 200$, and 250 (Figures 14(c) and 14(d)). It is to be noted that the variation trend of the St number with L/D is opposite to those of C_{Dmean} . There is a quick jump in St number for $Re = 150$ at $L/D = 7$. It was observed that two flow regimes (regime-I to regime-II) appear intermittently. The results further show that the Strouhal values are considerably lower than the isolated cylinder as the value of L/D increased. Generally, the St number of the square cylinder became lower than the isolated cylinder as the value of L/D increased. The slight increase in C_{Dmean} and quick decrease in Strouhal number is closely related to the wake structure changes behind the square cylinder.

It is seen from Figure 14(f) that, as the value of L/D increased, considerable changes in C_{Drms} are produced at $Re = 250$. It is noted that the effect of L/D on the C_{Drms} for $Re = 200$ and 250 (Figure 14(f)) as compared to $Re = 100$ and 150 (Figure 14(e)). The C_{Drms} for $L/D = 6$ to 8 at $Re = 250$ is much higher than that for a single square cylinder without T-shaped control plate (Figure 14(f)). In all other considered cases, the lift is smaller. As already discussed, flow features qualitatively above, when the L/D value increases, the C_{Lrms} increase. When the L/D value reaches a particular value, for example, 3.5 at $Re = 150$ (Figure 14(g)), there occurs a

maximum value. As L/D increases, C_{Lrms} increases first and reaches their maximum values for all Re values and then decreases (Figures 14(g) and 14(h)). It is found that, for $Re = 150$, 200, and 250 the maximum value occurs at $L/D = 3.5$, 3, and 3.5, respectively. The C_{Lrms} associated with the square cylinder with the upstream attached T-shaped control plate for $Re = 100$ is lower than that of the isolated cylinder.

The C_{Lrms} values at $Re = 250$ (Figure 14(f)) are more scattered and either increased or decreased while changing the value of L/D . It can be seen from Figure 14(e) that the cylinder with the upstream attached T-shaped control plate had lower values of C_{Lrms} than the isolated cylinder at $Re = 100$ as the value of L/D increased. This can be attributed to the main reason that the shear layers downstream of the square cylinder are delayed by the use of the upstream attached T-shaped control plate. It can also be clearly seen that, for $Re = 150$ by increasing L/D up to 2.5, the C_{Lrms} had a fixed value and considerably lower than the isolated cylinder value. However, by further increasing the length ($3 \leq L/D \leq 5.5$), C_{Lrms} increases and attains its maximum value and then starts to decrease slowly. In some specific cases, the value is more than the isolated cylinder. In general, increasing the length of T-shaped control plate from $L/D = 4$ onwards did not have a considerable effect on integral parameters.

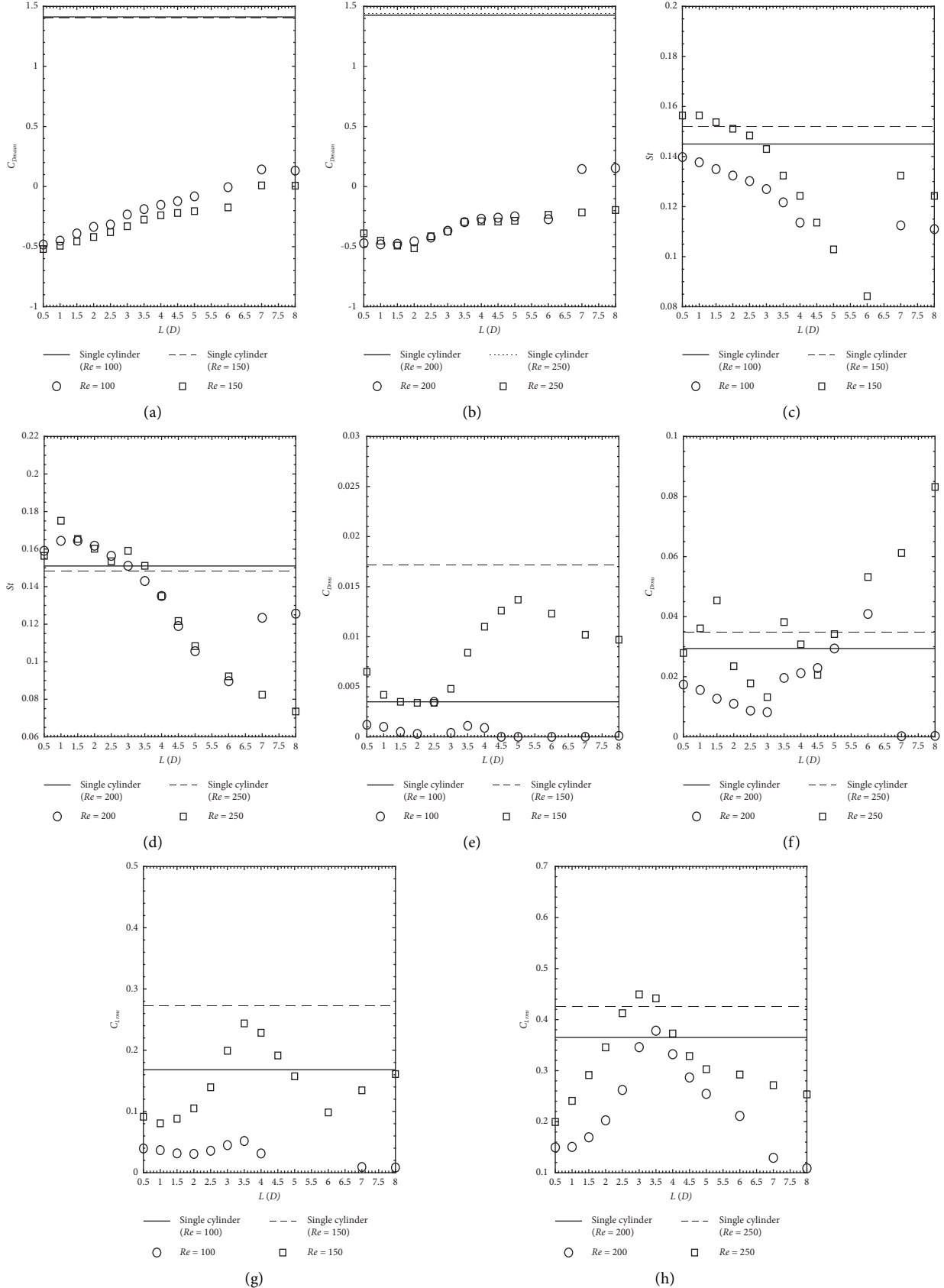


FIGURE 14: Variation of integral parameters of square cylinder with and without attached T-shaped control plate as a function of L/D at different fixed Re values: (a, b) $C_{D\text{mean}}$, (c, d) St , (e, f) $C_{D\text{rms}}$, and (g, h) $C_{L\text{rms}}$.

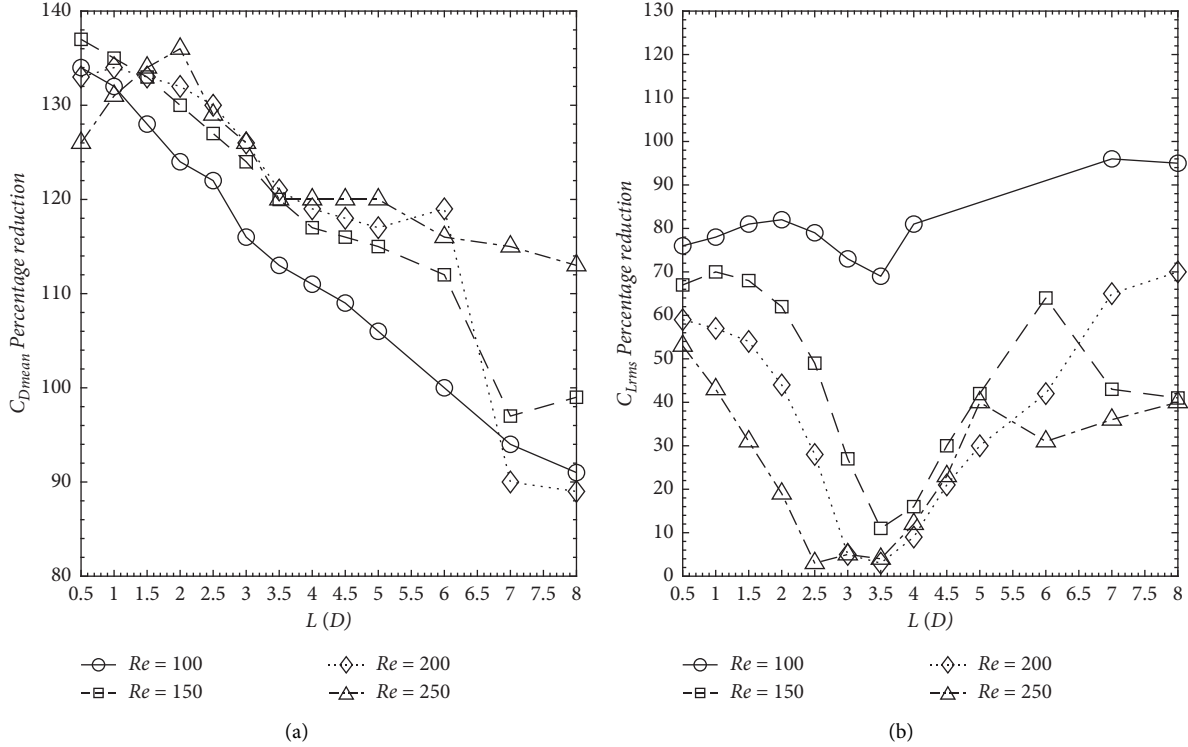
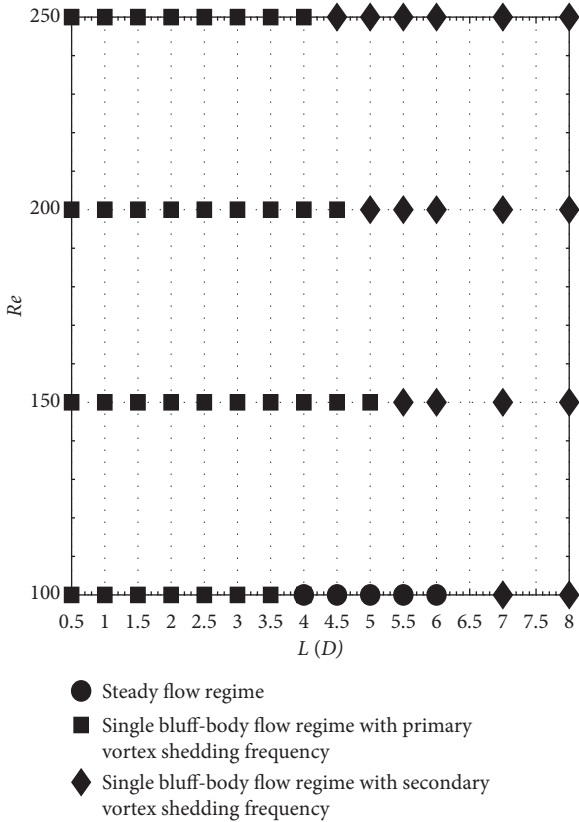
FIGURE 15: Percentage variation of (a) $C_{D\text{mean}}$ and (b) $C_{L\text{rms}}$ as a function of L/D at different fixed Re values.FIGURE 16: Flow regimes map as a function of L/D and Re .

TABLE 7: Wake length (L_r/D) of flow past a square cylinder in presence of upstream attached T-shaped control plate.

L/D	Re = 100	Re = 150	Re = 200	Re = 250
0.0	1.0	1.0	0.5	2.0
0.5	2.0	1.0	1.0	1.5
1.0	2.5	1.5	1.0	0.5
1.5	0.75	1.25	0.5	0.5
2.0	1.25	1.5	1.0	1.0
2.5	1.0	0.5	0.75	1.0
3.0	0.5	1.0	1.25	1.0
3.5	0.5	1.25	1.25	0.5
4.0	1.0	1.0	2.5	0.75
4.5	2.75	0.5	1.5	0.75
5.0	2.5	0.5	1.75	2.0
5.5	2.0	1.0	1.0	1.5
6.0	2.5	1.5	0.75	1.0
7.0	2.0	0.75	1.0	1.0
8.0	1.5	0.5	1.0	1.5

Figures 15(a) and 15(b) depicts the percentage variation of C_{Dmean} and C_{Lrms} for all the considered cases of T-shaped control plate length. It is noticed that, with increasing L/D , the percentage reduction in terms of C_{Lrms} increases. The previous studies suggest that the usually very small length of the splitter is good enough for maximum drag reduction and fluid forces suppression. Here we also observed that a small length ($L/D \geq 1.5$) of T-shaped control plate considerably reduced the drag forces. For example, at $Re = 250$, the reduction in C_{Dmean} is 126%, 131%, 134%, 136%, 129%, 126%, 120%, 120%, 120%, 116%, 115%, and 113% for the T-shaped plate with $L/D = 0.5, 1, 1.5, 2, 2.5, 3, 3.5, 4, 4.5, 5, 5.5, 6, 7$, and 8, respectively.

According to the values of L/D and Re and based on the investigation of the time-averaged and instantaneous vorticity contours visualization on the T-shaped control plate and square cylinder, three major flow regimes are found in this numerical study and shown in Figure 16. One flow regime, $L/D = 4.5$ to 6 at $Re = 100$, is a steady flow regime in which no vortex shedding is observed behind the square cylinder. Another flow regime is the single bluff body flow regime. In the case of a single bluff body flow regime, a regular von Karman vortex street is observed behind the main square cylinder. In the case of a single bluff body flow regime, we further observed two different flow regimes. Single bluff body with St_p and St_s . St_p and St_s stand for dominant primary vortex shedding frequency and secondary frequencies together with primary vortex shedding frequency, respectively. Single bluff bodies with St_p are found at $(L/D, Re) = (0.5-4, 100), (0.5-5, 150), (0.5-4.5, 200)$, and $(0.5-4, 250)$. Single bluff bodies with St_s are found at $(L/D, Re) = (7-8, 100), (5.5-8, 150), (5-8, 200)$, and $(4.5-8, 250)$.

The wake length (L_r/D) is quantitatively calculated and is given in Table 7. The data confirms that wake lengths changed as the value of L/D increased from 0.5 to 8. As shown, the L_r/D for all the considered L/D values is changed. For cases with $Re = 100$ and $4.5 \leq L/D \leq 7$, the more L_r/D values are observed due to steady flow behavior behind the square cylinder.

4. Conclusions

A two-dimensional unsteady fluid flow around a square cylinder with an upstream attached T-shaped control plate was investigated numerically, and the important findings were reported in the present study. The flow characteristics and fluid forces were examined at $Re = 100, 150, 200$, and 250. The length of the T-shaped control plate is varied. A considerable effect of T-shaped control plate on the fluid forces around the square cylinder is observed, and accordingly, the following important conclusions can be drawn from the present computation:

- (i) It was found from the present computations that the vortex street behind the square cylinder was still maintained, but there was a significant decrease in drag. Decreasing the length of the upstream attached T-shaped control plate had a considerable effect on reduction of drag coefficient and rms value of lift coefficient. However, for $L/D \geq 5$, it did not have a considerable effect on the fluid forces. The minimum C_{Dmean} was observed at $L/D = 0.5$ for $Re = 100, 150$, and 200 and at $L/D = 2$ for $Re = 250$. At $L/D = 0.5, 134\%, 137\%, 133\%$, and 136% reduction of C_{Dmean} was achieved for $Re = 100, 150, 200$, and 250, respectively. It was also found that when the length of T-shaped control plate is short, for instance, $L/D \leq 3$, the effect of the length of the T-shaped control plate on controlling the flow past a square cylinder becomes noticeable.
- (ii) A complete vortex shedding suppression for T-shaped control plate was achieved, at a T-shaped control plate length of $L/D = 4.5$ to $L/D = 6$ at Reynolds number 100. A maximum C_{Lrms} reduction of about 96% compared to the isolated cylinder was achieved at $Re = 100$ and $L/D = 7$ using T-shaped control plate. It was found that, as L/D increased, rms values of both drag coefficient and lift coefficient of square cylinder without T-shaped control plate considerably reduced compared with the isolated cylinder.
- (iii) Three different flow regimes were found in this study. The first one is the single bluff body flow regime with primary vortex shedding frequency (regime I). The second one is the single bluff body flow regime with secondary vortex shedding frequencies together with the primary vortex shedding frequency (regime II). The third one is the steady flow regime (regime III). In the case of regime-I, we found the dominance of primary vortex shedding frequency. On the other hand, in the case of regime-II, some extra minor peaks also exist in the power spectra.

Abbreviations

- C_D : Drag coefficient
- C_L : Lift coefficient
- C_{Dmean} : Mean drag coefficient

C_{Drms} :	Root-mean-square of drag coefficient
C_{Lrms} :	Root-mean-square of lift coefficient
c_s :	Speed of sound
Re :	Reynolds number ($Re = U_\infty D/v$)
St :	Strouhal number ($St = f_s D/U_\infty$)
St_p :	Strouhal number based on primary vortex shedding
St_s :	Strouhal number based on secondary vortex shedding frequencies
D :	Size of the main square cylinder
L :	Length of the T-shaped control plate
w :	Width of the T-shaped control plate head
f_s :	Vortex shedding frequency
U_∞ :	Uniform inflow velocity
L_u :	Upstream distance from the inlet position
L_d :	Downstream distance from the rear surface of the square cylinder
L_x :	Length of the computational domain
L_y :	Height of the computational domain
Ma :	Mach number
$f_i(\mathbf{x}, t)$:	Particle distribution function
$f_i^{(eq)}$:	Equilibrium distribution function
(\mathbf{x}, t) :	
p :	Pressure
ρ :	Density of the fluid
τ :	Single-relaxation-time parameter
δt :	Computational time-step
δx :	Lattice spacing
v :	Kinematic viscosity of the fluid
ω_i :	Weighting coefficients
e_i :	Discrete particle velocity
d :	Dimensions
q :	The number of particles
ω_z :	Vorticity
BGK:	Bhatnagar–Gross–Krook
LBM:	Lattice Boltzmann method
LGA:	Lattice gas automata
N-S:	Navier–Stokes
rms:	Root mean square
SRT:	Single-relaxation-time.

Data Availability

The data that support the main findings of this numerical study are available from the corresponding author upon request.

Conflicts of Interest

The authors declare that they have no known conflicts of interest that could have appeared to influence the numerical work reported in this study.

Acknowledgments

The second author Dr. Shams-ul-Islam is specially grateful to Higher Education Commission (HEC) Pakistan for providing funds under project no. 9083/Federal/NRPU/R&D/HEC/2017.

References

- [1] R. Abdi, N. Rezazadeh, and M. Abdi, “Reduction of fluid forces and vortex shedding frequency of a circular cylinder using rigid splitter plates,” *European Journal of Computational Mechanics*, vol. 26, no. 3, pp. 225–244, 2017.
- [2] S. U. Islam, R. Manzoor, Z. C. Ying, M. M. Rashdi, and A. Khan, “Numerical investigation of fluid flow past a square cylinder using upstream, downstream and dual splitter plates,” *Journal of Mechanical Science and Technology*, vol. 31, no. 2, pp. 669–687, 2017.
- [3] X. Zhou, J. Wang, and Y. Hu, “Experimental investigation on the flow around a circular cylinder with upstream splitter plate,” *Journal of Visualization*, vol. 22, no. 4, pp. 683–695, 2019.
- [4] K. R. Sharma and S. Dutta, “Effect of rigid and flexible splitter plate attached to square cylinder on Strouhal number at moderate Reynolds number,” in *Proceedings of the 24th National and 2nd International ISHMT-ASTFE Heat and Mass Transfer Conference (IHMTC-2017)*, Hyderabad, India, December 2018.
- [5] M. K. Chauhan, S. Dutta, B. S. More, and B. K. Gandhi, “Experimental investigation of flow over a square cylinder with an attached splitter plate at intermediate Reynolds number,” *Journal of Fluids and Structures*, vol. 76, pp. 319–335, 2018.
- [6] S. M. Dash, M. S. Triantafyllou, P. Valdivia, and Y. Alvarado, “A numerical study on the enhanced drag reduction and wake regime control of a square cylinder using dual splitter plates,” *Computers & Fluids*, vol. 199, pp. 1–13, 2020.
- [7] S. Soumya and K. A. Prakash, “Effect of splitter plate on passive control and drag reduction for fluid flow past an elliptic cylinder,” *Ocean Engineering*, vol. 141, pp. 351–374, 2017.
- [8] B. Barman and S. Bhattacharyya, “Control of vortex shedding and drag reduction through dual splitter plates attached to a square cylinder,” *Journal of Marine Science and Application*, vol. 14, no. 2, pp. 138–145, 2015.
- [9] K. R. Sharma and S. Dutta, “Flow control over a square cylinder using attached rigid and flexible splitter plate at intermediate flow regime,” *Physics of Fluids*, vol. 32, no. 1, p. 014104, 2020.
- [10] M. Sarioglu, “Control of flow around a square cylinder at incidence by using a splitter plate,” *Flow Measurement and Instrumentation*, vol. 53, pp. 221–229, 2017.
- [11] S. Kim, J.-C. Yoon, and B.-S. Yim, “Suppression characteristics of flow-induced vibration in a test cylinder with varying locations of a control cylinder,” *Journal of Mechanical Science and Technology*, vol. 32, no. 12, pp. 5685–5696, 2018.
- [12] S.-U. Islam, R. Manzoor, and A. Tareen, “Numerical investigation of flow around square cylinder with an upstream control plate at low Reynolds numbers in tandem,” *Journal of the Brazilian Society of Mechanical Sciences and Engineering*, vol. 39, no. 4, pp. 1201–1223, 2017.
- [13] K. R. Sharma and S. Dutta, “Influence of length and effective stiffness of an attached flexible foil for flow over a square cylinder,” *Journal of Fluids and Structures*, vol. 104, pp. 1–28, 2021.
- [14] E. Firat, Y. E. Akansu, and H. Akilli, “Flow past a square prism with an upstream control rod at incidence to uniform stream,” *Ocean Engineering*, vol. 108, pp. 504–518, 2015.
- [15] S.-C. Yen, S.-F. Wu, and K.-C. San, “Modulation of wake flow and aerodynamic behaviors around a square cylinder using an

- upstream control bar,” *Experimental Thermal and Fluid Science*, vol. 70, pp. 139–147, 2016.
- [16] H. Zhu and J. Yao, “Numerical evaluation of passive control of VIV by small control rods,” *Applied Ocean Research*, vol. 51, pp. 93–116, 2015.
 - [17] H. Zhu, J. Yao, Y. Ma, H. Zhao, and Y. Tang, “Simultaneous CFD evaluation of VIV suppression using smaller control cylinders,” *Journal of Fluids and Structures*, vol. 57, pp. 66–80, 2015.
 - [18] M. K. Chauhan, S. Dutta, and B. K. Gandhi, “Wake flow modification behind a square cylinder using control rods,” *Journal of Wind Engineering and Industrial Aerodynamics*, vol. 184, pp. 342–361, 2019.
 - [19] W. S. Abbasi, S. U. Islam, and H. Rahman, “Proximity effects on characteristics of flow around three inline square cylinders,” *Mathematical Problems in Engineering*, vol. 2019, Article ID 1752803, 14 pages, 2019.
 - [20] S. Ahmad and S. Ul-Islam, “Numerical investigation of fluid flow past four cylinders at low Reynolds numbers,” *Mathematical Problems in Engineering*, vol. 2021, Article ID 1127324, 24 pages, 2021.
 - [21] S. Rashdi, M. Hayatdavoodi, and J. A. Esfahani, “Vortex shedding suppression and wake control: a review,” *Ocean Engineering*, vol. 126, pp. 57–80, 2016.
 - [22] T. Kruger, H. Kusumaatmaja, A. Kuzmin, O. Shardt, G. Silva, and E. M. Viggen, *The Lattice Boltzmann Method: Principles and Practice*, Springer, Berlin, Germany, 2017.
 - [23] A. A. Mohamad, *Lattice Boltzmann Method: Fundamentals and Engineering Applications with Computer Codes*, Springer, Berlin, Germany, Second edition, 2019.
 - [24] Z. Guo, H. Liu, L.-S. Luo, and K. Xu, “A comparative study of the LBE and GKS methods for 2D near incompressible laminar flows,” *Journal of Computational Physics*, vol. 227, no. 10, pp. 4955–4976, 2008.
 - [25] D. Yu, R. Mei, L.-S. Luo, and W. Shyy, “Viscous flow computations with the method of lattice Boltzmann equation,” *Progress in Aerospace Sciences*, vol. 39, no. 5, pp. 329–367, 2003.
 - [26] S. C. Luo, X. H. Tong, and B. C. Khoo, “Transition phenomena in the wake of a square cylinder,” *Journal of Fluids and Structures*, vol. 23, no. 2, pp. 227–248, 2007.
 - [27] A. Okajima, “Strouhal numbers of rectangular cylinders,” *Journal of Fluid Mechanics*, vol. 123, pp. 379–398, 1982.
 - [28] C. Norberg, “Flow around rectangular cylinders: pressure forces and wake frequencies,” *Journal of Wind Engineering and Industrial Aerodynamics*, vol. 49, no. 1-3, pp. 187–196, 1993.
 - [29] A. Sohankar, L. Davidson, and C. Norberg, *Numerical Simulation of Unsteady Flow Around A Square Two-Dimensional Cylinder*, The University of Sydney, Sydney, Australia, 1995, https://www.researchgate.net/publication/292152601_Numerical_simulation_of_unsteady_flow_around_a_square_two-dimensional_cylinder.
 - [30] A. K. Saha, G. Biswas, and K. Muralidhar, “Three-dimensional study of flow past a square cylinder at low Reynolds numbers,” *International Journal of Heat and Fluid Flow*, vol. 24, no. 1, pp. 54–66, 2003.
 - [31] S. Dutta, P. K. Panigrahi, and K. Muralidhar, “Effect of orientation on the wake of a square cylinder at low Reynolds numbers,” *Indian Journal of Engineering and Materials Sciences*, vol. 11, pp. 447–459, 2004.
 - [32] C. Y. Zhou, L. Wang, and W. Huang, “Numerical study of fluid force reduction on a circular cylinder using tripping rods,” *Journal of Mechanical Science and Technology*, vol. 21, no. 9, pp. 1425–1434, 2007.